High surface area TiO2 photocatalyst for H2 production through silicon micromachining

Maria-Isabel Mendoza-Diaz, Aurélie Lecestre, Ludovic Salvagnac, Botayna Bounor, David Pech, Mehdi Djafari-Rouhani, Alain Estève, Carole Rossi

High surface area TiO_2 photocatalyst for H_2 production through silicon micromachining

Maria-Isabel Mendoza-Diaz, Aurélie Lecestre, Ludovic Salvagnac, Botayna Bounor, David Pech, Mehdi Djafari-Rouhani, Alain Esteve, Carole Rossi*

LAAS-CNRS, University of Toulouse, 7 Avenue du colonel Roche, 31400 Toulouse, France

* Corresponding Author.

E-mail: rossi@laas.fr, (C. Rossi). Tel. +33-05-6133-6301

Keywords: TiO_2, photocatalyst, 3D microstructure, DRIE, H_2 production, water splitting

Abstract. The development of an efficient photocatalyst capable of producing enough hydrogen for applications in everyday life under direct sunlight exposure is still challenging. In this work, a new concept for a three-dimensional microstructured photocatalyst is proposed, in which a standard deep-reactive ion etching process allows for the optimization, fabrication and subsequent deposition of TiO_2 thin films by physical vapor deposition for H_2 production by direct water splitting. After the development of enlarged surface microstructures, the composition and morphology of the 3D TiO_2 photocatalyst were characterized by XRD, XPS, UV/Vis spectroscopy and SEM. Furthermore, the influence of the area enlargement factor on the 3D photocatalyst surface morphology and its photocatalytic performance under UV-visible irradiation was thoroughly analyzed and corroborated by electrochemical experiments. The photocatalyst exhibited an increase in H_2 production by almost a factor of 12 compared to conventional planar TiO_2 films. The H_2 production was further improved by a factor of 4 through the introduction of Au nanoparticles grown on top of the TiO_2 layer. The advantages and development of robust and hierarchical photocatalysts using microelectromechanical fabrication techniques are highlighted as potential solutions for

a broad range of applications from photocatalysis, electronics, and sensing elements to 3D metamaterials.

1. Introduction

An attractive approach for the energy industry's transition to sustainable and clean energy is the use of solar radiation to produce hydrogen [1]. Among the different artificial photocatalytic processes, H_2 production through water splitting (WS) is probably the most intensely studied since H_2 exhibits a high volumetric energy density and no carbon footprint and can be either directly burned or used in fuel cells to produce electricity [2,3]. In 1972, pioneering work by Honda and Fujishima demonstrated that the water splitting into H_2 and O_2 could be achieved by irradiating light onto a titania (TiO_2) photoanode connected to a platinum cathode in an electrochemical cell [4]. A few years later, Borgarello et al. [5] demonstrated the feasibility of a bifunctional RuO/TiO_2 photocatalyst to achieve water splitting. The WS mechanism takes place when photoexcited electrons and holes act as reducing and oxidizing agents to produce H_2 and O_2, respectively (concept depicted in **Figure 1**) [6]. Since these seminal works, great progress has been made to understand the microscopic processes involved in photochemical systems and in catalyst engineering [7-8]. Among a large choice of proposed materials (nitride compounds [9,10] or composed Bi_2WO_6, TaON, Bi_2O_3, Ag_2O, Ag_3VO_4 [11-13]), titanium dioxide remains the most suitable catalyst for industrial applications due to its performance, easy accessibility, nontoxicity and low price [14]. However, its solar-to-hydrogen conversion efficiency remains low (~ 0.4% [15]), which is still far from the optimum efficiency required for practical use in the fuel cells of modern devices. Extensive research efforts are still being devoted to specifically extending the light absorption spectra to visible light ($\lambda > 400$ nm), either by doping TiO_2 with metals or plasmonic nanoparticles (Ag or Au) [16,17]. Another strategy to improve the hydrogen production rate is to augment the surface-to-volume ratio by creating high surface

microstructures [18,19]. This is especially of major importance when dealing with systems in which the photocatalytic area is limited. Despite is high cost, film technologies such as physical vapor deposition (PVD), offers a good solution for fabrication of films with great adhesion, compact and resistant [20].

To the best of our knowledge, a quantification of the photocatalytic activity improvement related to the electrode surface area enlargement has never been investigated. The present study proposes to use silicon micromachining technique to fabricate well-defined three-dimensional (3D) geometries of TiO_2 photocatalysts in order to relate the surface area with the H_2 production rate to drive the design of future electrodes. We designed and successfully created a well-defined and repeatable array of microcavities through a photolithography process which consists of the deep-reactive ion etching (DRIE) of silicon followed by the sputter deposition of a continuous layer of TiO_2. After developing the fabrication process of the 3D photocatalyst, the influence of the area enlargement factor (AEF) on the morphology, quality and catalytic performance of the 3D photocatalyst was thoroughly investigated. We show that the H_2 production rate can be improved ten times compared to a planar topology. Moreover, H_2 production is improved by a factor of four through the growth of Au nanoparticles inside the continuous TiO_2 catalytic layer, leading to a UV/visible synergistic effect, as discussed in previous works [21]. This work not only proposes a fabrication process that can be easily implemented in the fabrication of silicon-based microdevices which is of fundamental and technological interest for electronics, sensing elements to 3D photonics and metamaterials; but also presents a direct understanding by firmly establishing a relation between the surface area augmentation and the photocatalytic properties of electrodevices.

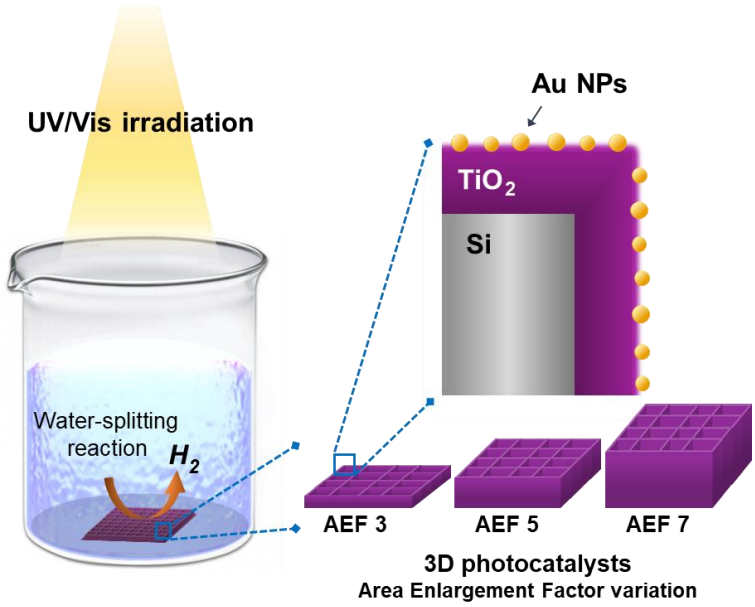

Figure 1. *Conceptual scheme of the 3D microstructured photocatalyst with variant AEF immersed in water to produce H_2 under sunlight irradiation for water splitting applications. Insert: cross-section of the photocatalyst (gray: silicon, violet: TiO_2 and yellow: gold nanoparticles).*

2. Materials and methods

2.1 Silicon microstructure

A 500 µm thick, single-side-polished, 4-inch silicon p-type substrate was chosen for the fabrication of the microstructures that will serve as the experimental substrates. The technological process is composed of four main steps, as depicted in **Figure 2**: photolithography, silicon etching by DRIE, postprocessing obtainment of a smooth silicon scaffold and deposition of the catalytic thin layer.

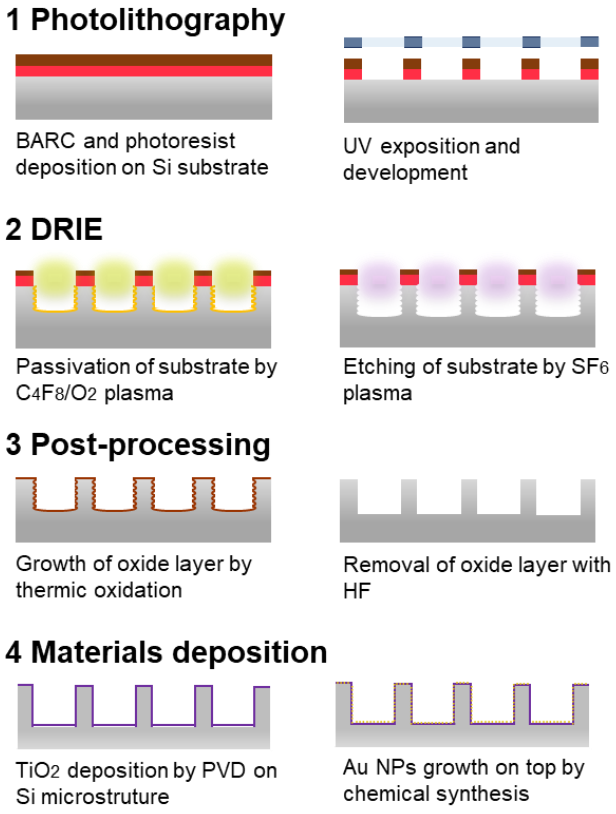

Figure 2. *Main process steps underlining the cross-section of the 3D photocatalyst: (1) photolithography; (2) deep reactive ion etching where consecutive cycles of SF_6 and C_4F_8/O_2 steps etch and passivate the silicon; (3) postprocessing by thermal oxidation of silicon followed by the removal of the oxide layer; and (4) TiO_2 layer sputter deposition followed by (optional) chemical synthesis of Au nanoparticles.*

Photolithography. As a first step, a bottom anti-reflective coating layer (BARC, MicroChemicals) is deposited by spin-coating and baked at 200 °C for 1 min. Next, a positive photoresist (denoted PR; AZ-40XT, MicroChemicals, 20 µm) is spin-coated onto the silicon wafer and patterned using photolithography. This PR layer is "soft baked" from 65 to 126 °C for 1.5 min and cooled to room temperature. The PR layer is then patterned by exposing it for 10 s to UV light (A6 Gen4 Suss Microtec) shone through a patterned contact mask. The patterning of the PR layer is completed by developing the exposed PR with a MF-CD-26

developer for 120 s, followed by rinsing in deionized water and drying with N_2. The PR layer is finally "hard baked" from 65 to 105 °C for 80 s.

Deep Reactive Etching (DRIE). Silicon etching was performed using an AMS420 reactor manufactured by Alcatel-Adixen. Etching and passivation cycles of SF_6 and C_4F_8/O_2 gases are set to a constant flow rate (**Table 1**) and variable exposure time for each gas, the latter of which will be presented in Section 4.

Table 1. *Detail of DRIE main process parameters.*

Gases	Flow (l min^{-1})	Power (W)
SF_6	0.25	2500
C_4F_8/O_2	0.25/0.035	2500/70

Post-processing. To remove the scalloping trenches from the cavity walls and obtain a smooth silicon surface, the silicon microstructures undergo a thermic oxidation process that consists of growing a 1 µm thick SiO_2 layer that uniformly covers all the trenches, which is subsequently removed. The thermal oxidation treatment is composed of four steps: first, a preoxidation step of 30 min at 1070 °C under O_2 (10 L/min), followed by a wet oxidation step for 145 min under a mixture of O_2/H_2 (6/10 L/min), a dry-oxidation step for 60 min under O_2 (10 L/min), and the oxidation phase by annealing for 15 min in a neutral N_2 atmosphere (10 L/min); then, a cooling down step with a ramp of - 4 °C/min down to 700 °C under N_2. Finally, the SiO_2 layer is removed chemically with HF solution.

2.2 TiO_2 sputter-deposition

TiO_2 was sputter-deposited by direct current magnetron sputtering of a Ti target (99.999% purity). The pressure of the chamber was 8×10^{-8} Pa. A gas mixture of 40% O_2 and 60% Ar

was set with a pressure of 1.07 Pa. The DC power of reactive plasma was 1200 W. Three different thicknesses were sputter-deposited on the silicon microstructures, being these 270, 650 and 1000 nm (measured on flat surface), named T1, T2 and T3, respectively.

2.3 Grafting of Au nanoparticles

To improve the H_2 production rate of the TiO_2 layer deposited on the microstructures, gold nanoparticles (Au NPs) are grown on the semiconductor film as described in [16] and [17]. Au NPs were synthesized through a photodeposition process under UV irradiation (365 nm, 100 W for 30 min) using a gold chloride trihydrate (III) acid ($HAuCl_4.3H_2O$ ≥99.9%, Sigma–Aldrich) aqueous solution (50 ml, 2.5×10^{-4} mol/l), a stabilizing agent of trisodium citrate dihydrate ($Na_3C_6H_5O_7.2H_2O$ 99.0%, Alfa Aesar) solution (5 mL, 0.05 mol/l), and ethanol (99.9%, Technic) as a sacrificial agent (5 mL) [17, 18]. An annealing step under air at 200 °C for 10 min is used to remove the organic ligands that surround the NPs and thus obtain chemical bonding to the TiO_2 surface. The stabilizing agent residuals were removed by rinsing with deionized water.

2.4 Characterization

The characterization methods included scanning electronic microscopy (SEM, FEI Helios 600i Nanolab), grazing incidence X-ray diffraction (GI-XRD, Bruker D8 Discover system), X-ray photoelectron spectroscopy (XPS, ESCALAB 250 X-ray photoelectron spectrometer) and UV/Vis absorption spectroscopy (Perkin-Elmer Lambda 650 Spectrometer). For photocatalytic experiments, the samples were placed into a quartz reactor (60 mL) filled with an aqueous solution (10 mL, 35% v/v ethanol) and connected to a gas chromatography apparatus (GC, Perkin-Elmer Clarus 580) to measure the H_2 production rate. The sample was irradiated by a Xenon light lamp (Cermax® PE300B-10F) with a spectral region of 300 to 1100 nm. The quantity of released hydrogen was monitored every 6 h. The hydrogen

evolution rate was normalized with respect to the light flux received by the sample, corrected for the UV absorption and calculated after 24 h of irradiation. Details are given in the Supplementary File (**Figure S1)**.

The area enlargement factor is obtained using electrochemical measurements carried out in a three-electrode configuration using a VMP-3 (Biologic) potentiostat operated with EC-Lab software. A platinum mesh and a silver chloride electrode (Ag/AgCl) were used as counter and reference electrodes, respectively. The Si/TiO_2 photocatalysts were covered with a film of Ti/Au (50 nm and 700 nm) by sputtering. The electrochemical active surface area (EASA) of the deposited gold was then calculated using the charge associated with the reduction of gold oxide in cyclic voltammetry experiments: a value of 390 $\mu C/cm^2$ in 0.5 M H_2SO_4 [25, 26]. The electrochemical AEF is defined as the ratio of the EASA of the microstructures to the EASA of a flat reference sample composed of silicon and 1 µm thick TiO_2 covered with a thin film of Ti/Au (50 nm and 700 nm).

3. Theoretical considerations

This section is devoted to the theoretical design with regard to the surface area enhancement of the optimum tunable pattern, which will be subsequently fabricated by silicon micromachining before further coating with the catalytic layer (**Figure 1**). The 3D photocatalyst was designed with a planar area of 1 cm^2. It is important that the aspect ratio can be tuned precisely in order to allow for the quantification of the H_2 production rate as a function of the total surface area.

The following patterns were studied for the microstructures (**Figure 3)**: square microcavities (hereafter denoted as microcavities), walls, pillars, rods and hollow-rods. Each pattern is characterized by a dimensionless geometric factor, *g*, which is used for the AEF calculation (**Equation 1**). The expression of *g* as a function of the main geometrical parameters (*a*, *w* and *depth*) that correspond to each pattern is given in **Figure 3**.

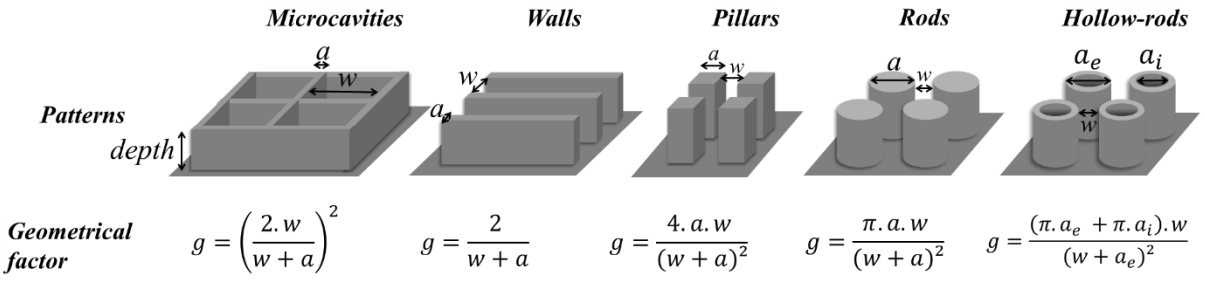

Figure 3. *3D view of the proposed patterns: microcavities, walls, square pillars, rods and hollow-rods, with their respective geometrical parameter g defined by the horizontal dimensions w and a.*

Then, the AEF can be calculated using the following equation:

$$\text{AEF} = 1 + g\left(\frac{depth}{w}\right) \qquad \text{Equation 1}$$

where *w* is the width of the features (width, diameter or spacing as specified in **Figure 3**) and *depth* is the depth of the etching. Obviously, technological restrictions must be considered in the variation of the geometrical parameters *a, w* and *depth.* Aside from the limitations of the photolithography resolution (10 µm) and silicon etching processes (critical aspect ratio due to DRIE process), the major restriction comes from the magnetron sputtering technique that is used to deposit the TiO_2 thin layer. To ensure continuous sputter deposition of the TiO_2 semiconductor film on the 3D micropatterned silicon substrate, an aspect ratio ≤ 2 is imposed. Therefore, a maximum *depth* of 150 µm and *w* of 75 µm are set to ensure this maximum aspect ratio for all the patterns. The influence of the geometrical parameter *a* on the AEF for the different patterns is plotted in **Figures 4a-b**. Note that the aspect ratio restriction also imposes the restriction $a \geq 10$ µm. For example, when *a* equals 10 µm, a microstructure composed of pillars or rods cannot achieve an AEF greater than 4, whereas microcavities achieve the highest surface enhancement with an AEF equal to 7 the *depth* equals 150 µm.

The wall pattern is not an efficient design to maximize the surface-to-volume ratio since the AEF is limited to 4.5.

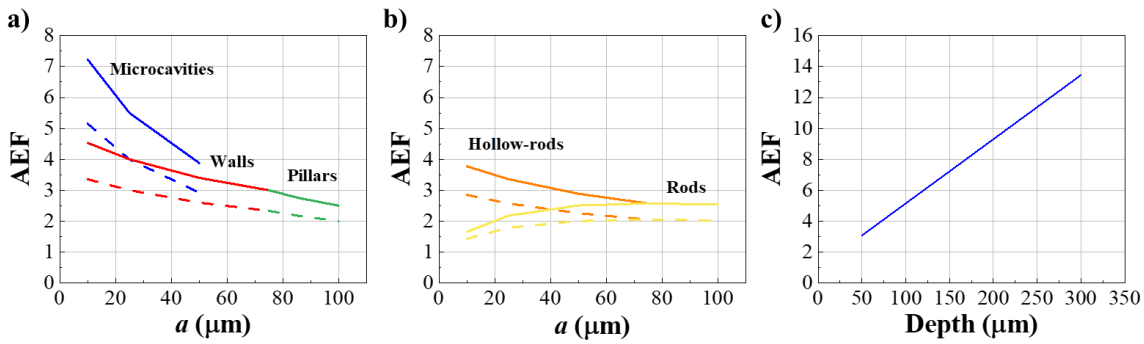

Figure 4. *Impact of the geometrical parameter a on the area enlargement factor (AEF) calculated using Equation 1 for: microcavities, walls, square pillars (a), hollow-rods, and rods (b)at depths of 100 (dashed line) and 150 µm (solid line). The parameter w is set at 75 µm to maintain a maximum aspect ratio of 2 for all the patterns. (c) Impact of depth on the AEF for the square microcavity pattern where w and a are 75 and 10 µm, respectively.*

Therefore, for 3D photocatalyst fabrication, we selected the microcavity pattern with dimensional parameters of 10 and 75 µm for *a* and *w*, respectively. Moreover, since the AEF is correlated to *depth* (**Figure 4c**), several silicon etching depths will be investigated. Indeed, the AEF is predicted to change from 3 to 7 when the microstructure depth goes from 50 µm to 150 µm.

4. Results and discussion

4.1. Silicon microstructures fabrication

An array of microcavities is fabricated into a 550 µm thick silicon p-type substrate using the DRIE process, as presented in Section 2. Control over the profile and *depth* is achieved by tuning the ratio of the exposure times of SF_6 to C_4F_8/O_2 gases, which corresponds to the passivation and etching steps in the DRIE process, respectively. **Figure 5** shows the SEM

cross-sections of the etched microcavities for different SF_6:C_4F_8/O_2 exposure time ratios. **Table 2** details the DRIE parameters and their corresponding profile characteristics. The profile angle θ, which describes the slope of the cavity wall edge, is calculated from the bottom and top widths of the wall and the cavity depth as described in Supplementary File, **Section 2**. When $\theta < 90°$, the profile is labeled negative (closing cavity), and when $\theta > 90°$, the profile is labeled positive (opening cavity).

At a SF_6:C_4F_8/O_2 exposure time ratio of 1.67 (SF_6:C_4F_8/O_2), the etch rate was 4.35 μm/min, but dropped to 1.75 μm/min when the SF_6:C_4F_8/O_2 exposure time ratio was 0.40. This difference in etch rates is due to the concentration of free fluorine radicals (F*) in the etching step in comparison to the concentration of free oxygen radicals (O*) that passivate the surface. Consequently, when the SF_6:C_4F_8/O_2 exposure time ratio is 0.40, the etching process is overcome by the passivation step, and the quantity of SiF_4 formed in each iteration is reduced, meaning that fewer silicon atoms are removed from the substrate.

Table 2. *Etch rate, profile angle θ and defects for different SF_6 and C_4F_8/O_2 exposure times in the DRIE process of silicon.*

Exposure time (s)		**SF_6:C_4F_8/O_2**	**Etch rate**	**Profile**		
SF_6	**C_4F_8/O_2**	**Ratio**	**(μm/min)**	**Angle θ (°)**	**Description**	**Grass defects**
2.5	1.5	1.67	4.35	89.19	Negative	No
2.2	2.0	1.10	4.17	89.63	Negative	No
1.7	2.0	0.85	2.65	89.79	Negative	No
1.5	2.0	0.75	3.00	90.28	Positive	No
2.0	3.5	0.57	2.69	90.97	Positive	Low density
2.0	5.0	0.40	1.75	91.79	Positive	High density

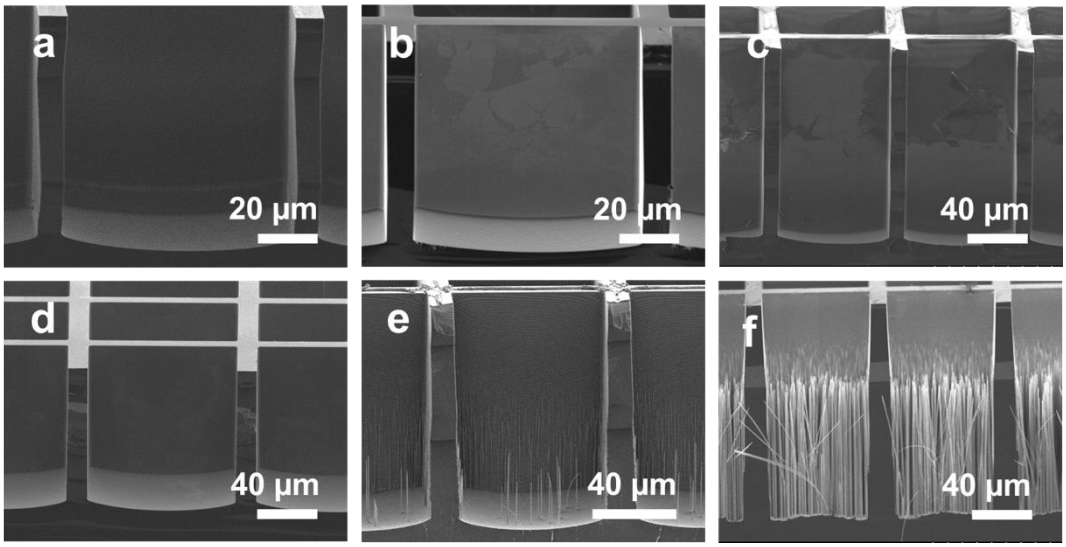

***Figure 5**. SEM cross-section images of silicon microstructures obtained by DRIE with SF_6:C_4F_8/O_2 exposure time ratios of 1.67 (a), 1.10 (b), 0.85 (c), 0.75 (d), 0.57 (e) and 0.40 (f). The depths are 74 µm (a), 75 µm (b), 127 µm (c), 75 µm (d), 109 µm (e) and 140 µm (f).*

Along with the etch rate, the profile is also highly influenced by the SF_6:C_4F_8/O_2 exposure time ratio. Beyond 0.85, negative profiles are obtained, as observed in **Figures 5a-c**. After decreasing to 0.75, the sidewalls become positive with a near vertical profile angle of 90.28° (**Figure 5d**). Below 0.57, positive profiles are obtained as well (**Figures 5e-f**). It should be noted that for each process case, the same profile geometry is observed over the entire substrate, demonstrating the uniform consistency of the micromachining process. To understand the impact of the SF_6:C_4F_8/O_2 exposure time ratio on the profile, it is important to explain the etching and passivation mechanisms that are inherent to the Bosch DRIE process used in this study. During the etching step, anisotropic accelerated ions remove the fluorocarbon layer that is located only at the bottom–of the cavities; next, isotropic etching takes place, removing the exposed silicon in all directions (detail in **Figure S3)**. This produces scalloping defects [22] with trenches that extend horizontally along the walls of the cavities, creating a completely corrugated surface, as observed in **Figure S4**. For higher concentrations of F* radicals (SF_6:C_4F_8/O_2 exposure time ratio ≥ 0.85), anisotropic sputtering

is favored since the passivation layer is scavenged quickly and the F* ions bounce repeatedly in the already etched trenches, removing the passivating layer and etching slightly more in each iteration, thus increasing the bottom diameter and forming a negative profile. **Table S1** gives the dimensions of the trenches that characterize the scalloping defects for the different SF_6:C_4F_8/O_2 exposure time ratios: the trench dimensions vary from 35 to 66 and 47 to 118 nm for horizontal and vertical ratios, respectively, with SF_6:C_4F_8/O_2 exposure time ratios ranging from 0.40 to 1.67.

For SF_6:C_4F_8/O_2 exposure time ratios below 0.57, the appearance of peaks is quite evident; this defect is also known as *grass*. For an SF_6:C_4F_8/O_2 exposure time ratio of 0.57 (**Figure 5e**) after an etch time of 26 min, the number of peaks is ~13 per cavity, whose height and width at the half-height are 22.4 μm and 0.44 μm on average, respectively. Below an SF_6:C_4F_8/O_2 exposure time ratio of 0.40, after an etch time of 80 min, the density of peaks increases drastically, as the *grass* covers the entire bottom surface of the cavities (**Figure 5f**): this results in what it is known as *black silicon*. Here, the silicon grass features an average height and width of 87.6 and 0.93 μm, respectively. Upon increasing the SF_6:C_4F_8/O_2 exposure time ratio above 0.75, no *grass* was formed (**Figure 5a-d**). Grass formation originates from the localized high concentration of oxide reaction products that are not removed from the surface before each new etch/passivation cycle [22]. This contamination acts as a *micromask* that creates a peak that is passivated and, due to isotropic etching, becomes higher with each iteration.

As a concluding remark for this technological study, an SF_6:C_4F_8/O_2 exposure time ratio of 0.75 will be used in the DRIE process to fabricate the microstructures, as it permits vertical walls with no grass defects to be obtained, thus ensuring good coverage and quality of the sputter-deposited TiO_2 onto the microcavities. Note that the presence of the scalloping defect inherent to the Bosh process remains, producing a corrugated surface along the walls. The

presence of such irregularities could generate a noncompact conformal TiO_2 layer, as the sputtering technique is highly dependent on the morphology and roughness of the substrate. To remove the scalloping, a 1 µm oxide layer was grown by thermal oxidation throughout the microstructure and subsequently etched with HF. The cross-sectional images in **Figure 6** show smooth edges and surfaces, which demonstrates the efficiency of the postprocessing step to remove scalloping defects while maintaining high-depth microstructures with a vertical profile. **Figure S5** shows additional SEM images of the microstructures which confirm that the roughness from the bottom cavity is reduced as well, and that the depth of the trenches on the walls is barely noticeable. The etch rate diminishes from 3.0 to 2.74 µm/min when working with an aspect ratio of 2.14, i.e., up to a depth of 150 µm, which represents a reliable high etch rate.

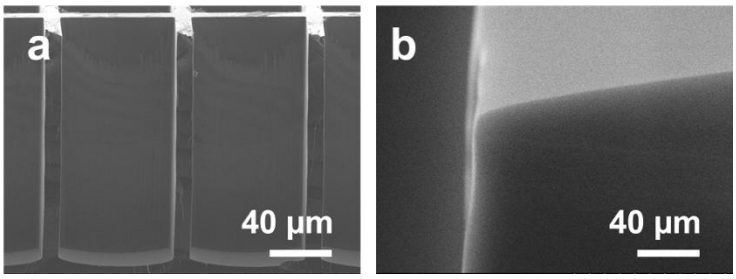

Figure 6. *SEM cross-section images of silicon microstructures after postprocessing: details of several microcavities (a) and a magnified view of an upper wall corner (b). DRIE process SF_6 and C_4F_8/O_2 exposure times of 1.5 and 2.0 s, respectively. The measured geometrical parameters are depth = 156 µm, w = 75 µm and a = 10.4 µm.*

4.2. 3D photocatalyst characterization

To study the impact of the enlarged surfaces of TiO_2 on the H_2 production rate, silicon microstructures were fabricated with defined AEFs of 3, 5 and 7, which correspond to microcavity depths of 50, 100 and 150 µm. **Table S2** details the measured geometrical

parameters for each of the microstructures used in this section. Next, a film of TiO_2 was deposited on top. Hereafter the AEF will be denoted in the name of the samples as A1, A3, A5 and A7; similarly, the TiO_2 thickness is indicated by T1, T2 and T3, as specified on the Materials and methods Section. Note that TiO_2 was also deposited on flat silicon where the AEF is 1. Sample A1-T2 with a thickness of 270 nm will be denoted as the reference sample due to its optimum photocatalytic performance, as was previously reported [21]. **Table 3** summarizes the set of samples having been classified by increasing AEF and presents the TiO_2 film thickness, which will be discussed later.

Table 3. *Details of TiO_2 thickness for the 2D and 3D photocatalysts featuring a variable AEF.*

			TiO_2 film thickness (nm)			
Sample	**AEF**	**Depth**	**Top**	**Bottom**	**Wall***	**Average thickness (t_{TiO2}^{av})**
A1-T1	1.00	0	-	100.00	-	-
A1-T2	1.00	0	-	270.00	-	-
A1-T3	1.00	0	-	650.00	-	-
A3-T1	3.08	50	283.11	129.73	80.08	108.02
A3-T2	3.08	50	573.32	224.68	203.83	237.22
A3-T3	3.08	50	1174.75	453.83	361.95	446.99
A5-T1	5.15	94	306.79	103.24	70.28	86.02
A5-T2	5.15	94	644.76	135.80	175.96	191.26
A5-T3	5.15	94	1105.00	246.50	278.65	311.44
A7-T1	7.23	156	285.77	33.87	60.75	65.17
A7-T2	7.23	148	697.13	69.66	137.43	143.33
A7-T3	7.23	148	1171.88	103.47	209.99	229.79

*Average calculated from the top, medium and bottom heights of the wall thickness.

TiO_2 structure, average thickness and surface morphology.

Characterization of the crystalline structure, optical absorbance and chemical composition were carried out only for the reference sample, as all the photocatalysts have the same TiO_2 composition, and the variation in thickness from 270 nm to 1 µm does not significantly affect the characterized properties. The GI-XRD pattern of deposited TiO_2 (**Figure 7a)** shows the characteristic peaks of anatase at 2θ = 25.24° for the (101) plane and of rutile at 2θ = 27.39° for the (110) plane, with the composition of each phase being 77.15% and 22.85%, respectively. The absorption spectra of the TiO_2 film deposited on quartz (**Figure 7b**) confirm the strong absorption of TiO_2 in the UV range from 200 to 349 nm. XPS results (**Figures 7c-d**) are consistent with XRD and UV/Vis observations. The signals in the Ti 2p and O 1s spectra have a stochiometric signature which corresponds to TiO_2. The O 1s peak is deconvoluted into two peaks, where the main component at 530.3 eV is the typical signal of the oxygen lattice of the O^{2-} bound to Ti^{+4} in TiO_2, and the other component at 531.02 eV can be assigned to weakly adsorbed oxygen species, subsurface low-coordinated oxygen ions, surface hydroxyl groups and/or carbonate species. The Ti 2p spectrum exhibits the characteristic spin-orbit splitting with the Ti $2p_{2/3}$ and $2p_{1/2}$ peaks. The contribution of the Ti^{4+} and Ti^{3+} components in the Ti $2p_{2/3}$ peak, are located at 457.3 and 456.5 eV; and in the $2p_{1/2}$ peak, the components are located at 466.05 and 464.8 eV, respectively [23-24].

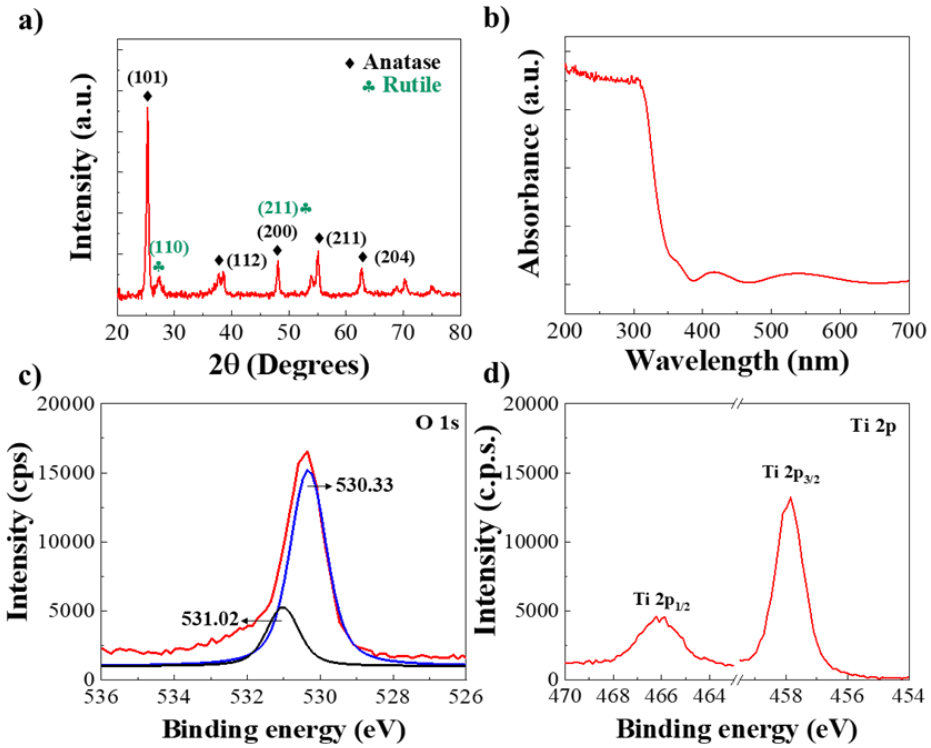

Figure 7. *Characterization of a 270 nm sputter-deposited TiO_2 film on a flat silicon substrate (samples A1-T2): (a) GI-XRD pattern, (b) UV–Vis absorption spectra (film deposited on quartz), XPS spectra, (c) O 1 s, and (d) Ti $2p_{1/2,3/2}$ regions.*

SEM observations of the 3D photocatalysts (**Figure 8**) show a continuous and compact layer for all samples, i.e., microstructures with aspect ratios of 0.7:1, 1.3:1 and 2:1, corresponding to AEFs of 3, 5 and 7, respectively. The cross-sectional images in **Figure 8** show the columnar growth of TiO_2, which is characteristic of the sputtering process. The grain growth was the same for all the fabricated photocatalysts, and the growth direction was merely influenced by the substrate surface position with respect to the PVD Ti target. This means that on the horizontal surfaces of the microcavities, i.e., the bottoms of the cavities, and at the top surfaces of the walls, the crystallites exhibit vertical growth (**Figures 8c, f and S6-7**), whereas on the vertical walls, the crystallite growth follows a diagonal direction (**Figures 8b, e and S8**). **Figures S6 and S8** show the cross-sectional details of the film at the bottoms of the cavity, the tops of the walls and at the half-height for each microstructure.

Moreover, the grain size also changes with variations in thickness. Due to its columnar growth, the upper diameter of the grain increases. By measuring the cross-sections on the top surface of the microcavities, the average grain upper diameter is 50.8, 95.0 and 153.8 nm for thicknesses T1, T2 and T3 (270, 650 and 1000 nm). Likewise, the size of the grains located at the bottom of the cavity and on the walls changes according to the layer thickness. For example, for sample A3-T3, the layers at the half-height of the wall and bottom of the microcavities are 380 and 336 nm, and the grain diameters are 61.5 and 50.2 nm, respectively.

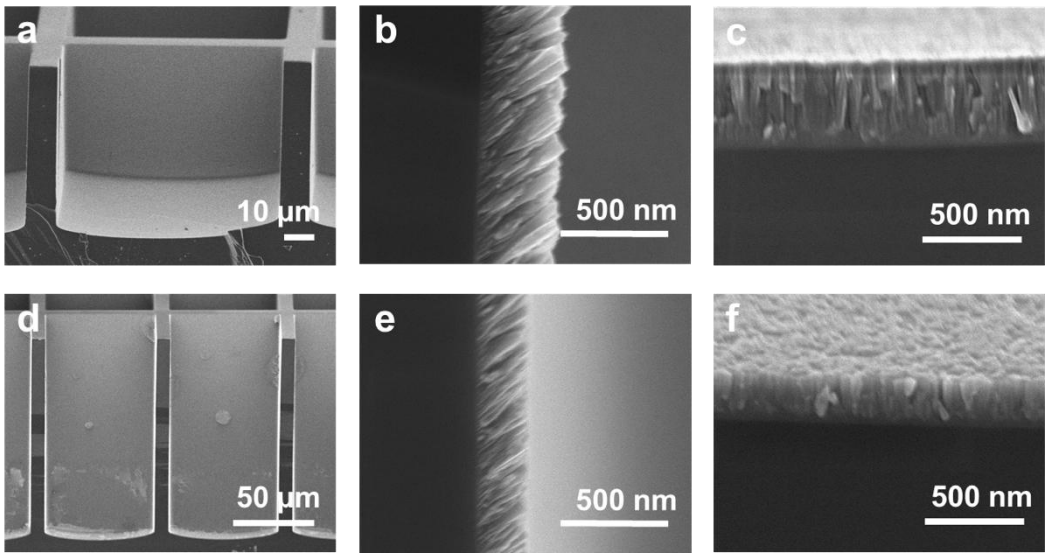

Figure 8. *SEM cross-sectional images of the 3D photocatalyst composed of silicon microstructures and TiO_2 film, corresponding to samples A3-T2 (a-c) and A7-T2 (d-f) featuring AEFs of 3 and 7, respectively. Details of the compact TiO2 layer at half-heights of the wall (b, e) and bottom of the microcavities (c, f).*

In addition, it is evident that the TiO_2 thickness deposited on the microstructures is not uniform with respect to the depth of the microcavities. As presented in **Table 3**, the thickness on the horizontal surfaces decreases from the top to bottom of the microcavities by a factor of 2.4, 4.0 and 9.9 for AEF values of 3, 5 and 7, (i.e., *depths* of 50 µm, 100 µm and 150 µm) respectively. On the vertical surfaces, the TiO_2 thickness decreases from the top to bottom of

the walls by a factor of 1.9, 3.4 and 6 for AEF values of 3, 5 and 7, respectively. Nevertheless, the TiO_2 layer remains compact and dense throughout the surface. This variation in thickness comes from the fact that, during the deposition in the sputtering process, the substrate is moving in front of the target in a parallel manner, and the atoms reach the sidewalls and corners more frequently due to the periodic high oblique angles of the incident flux.

To quantify the influence of the AEF on the photocatalytic activity, it is crucial to define an average thickness ($\boldsymbol{t_{TiO2}^{av}}$) of TiO_2 to distinguish each sample. In this regard, we use **Equation 2**, which accounts for the thicknesses measured at the top and bottom surfaces, and the average thickness deduced along the wall height; these values are then multiplied by a surface factor (**Table S3**) that represents the percentage of the total microstructure surface. Details are described in the Supplementary File, **Section S4**.

$$\boldsymbol{t_{TiO2}^{av}} = t_1 \cdot F1_{AEF} + t_2 \cdot F2_{AEF} + t_3 \cdot F3_{AEF} \qquad \text{Equation 2}$$

Where:

- $t_1, t_2\ and\ t_3$ are the averages of the TiO_2 thickness measured on the top, bottom surfaces and along the wall height, respectively.
- $F1$ is a factor defined by the AEF that represents the percentage of the total surface that is located at the horizontal top of the microstructure.
- $F2$ is a factor defined by the AEF that represents the percentage of the total surface that is located at the horizontal bottom of the microstructure.
- $F3$ is a factor defined by the AEF that represents the percentage of the total surface that is located on the walls of the microstructure.

Thus, the calculated average TiO_2 thickness for the 3D photocatalysts is reported in **Table 3**. Primarily, $\boldsymbol{t_{TiO2}^{av}}$ is thicker in the 3D photocatalyst with an AEF of 3, which is attributed to the

low aspect ratio of 0.7:1 of the microstructure. We also observe that the $\boldsymbol{t_{TiO2}^{av}}$ has a similar value with regard to the wall thickness in all the samples, which is attributed to the utilization of *F3* in Equation 2, which represents the percentage of the total surface that is located on the walls of the microstructure, and this value is 0.67, 0.84 and 0.86 for AEF values of 3, 5 and 7, respectively. This suggests that the film quality of the overall 3D photocatalysts is determined principally by the layer thickness on the walls. Another important observation is that for AEFs 3 and 5, the bottom of the microcavities has a higher thickness than the walls, which is contrary to AEF 7, and can be attributed to the limitation of the sputter deposition technique in reaching the bottom of the microcavities.

H_2 production rate. The photocatalytic H_2 production of the 3D photocatalysts was evaluated over 24 h under UV-vis irradiation. **Figure S9** shows the H_2 evolution over 24 h for each photocatalyst. Note that for the reference sample (A1-T2, flat photocatalyst), the quantity of H_2 evolution is linear over 24 h, whereas for sample A1-T3 and the 3D photocatalysts, the H_2 production remains constant only after 6 h of irradiation. Furthermore, for the different AEFs from 3 to 7, the photocatalysts with T3 thickness have a remarkedly higher H_2 production rate than T1 (i.e., increased by a factor of 57, 22 and 28 for AEFs 3, 5 and 7, respectively). This shows that the surface area enlargement not only impacts the H_2 production rate but also prominently impacts the TiO_2 layer, which, as discussed in the previous section, has a fluctuating thickness. Therefore, it is important to consider this characteristic for the interpretation of results. When considering the photocatalysts with thickness T1 that have a t_{TiO2}^{av} = 65.17 to 108.02 nm, the highest H_2 production rate was observed for sample A5-T1 with 0.018 μmol W^{-1} h^{-1}. This represents a 5-factor increase compared to A1-T1 (100 nm thickness), followed by A3-T1 rate of 0.009 μmol W^{-1} h^{-1}. Next, considering photocatalysts with thickness T2, with a t_{TiO2}^{av} = 143.33 to 237.22 nm, sample AEF5-T2 has the highest H_2 production rate with 0.196 μmol W^{-1} h^{-1}, which represents a 5-factor increase compared to the

reference sample (A1-T2 of similar thickness 270 nm), followed by A3-T2 with a rate of 0.167 µmol W^{-1} h^{-1}. Among the photocatalysts with T3 thickness, the flat A1-T3 (650 nm thickness) shows a high rate of 0.313 µmol W^{-1} h^{-1}; nevertheless, for the purpose of comparison within the 3D photocatalysts that have a t_{TiO2}^{av} = 229.79 to 446.99 nm, it is necessary to use a reference sample with a similar thickness, such as sample A1-T2; in this regard, samples A3-T3 and A5-T3 exhibit a remarkable 12-factor and 10-factor enhancement of with H_2 production rates of 0.5 and 0.393 µmol W^{-1} h^{-1}, respectively; moreover, their H_2 evolution exhibits the fastest rate during the 24 h tests. In addition, the quantum efficiency (QE) of the optimal 3D TiO_2 photocatalysts (thickness T3) was calculated considering the spectral output of the Xe lamp. Details are given in the Supplementary File, **Section 6**. The QE for samples A3-T3, A5-T3 and A7-T is 8.74, 7.24 and 6.29%, respectively. Due to a low power irradiation of the lamp, comparison with literature is relatively difficult. Yet, we can deduce that the enhanced photon-to-H2 production is caused by the area enlargement of the 3D photocatalysts under the same irradiation and with the same planar area.

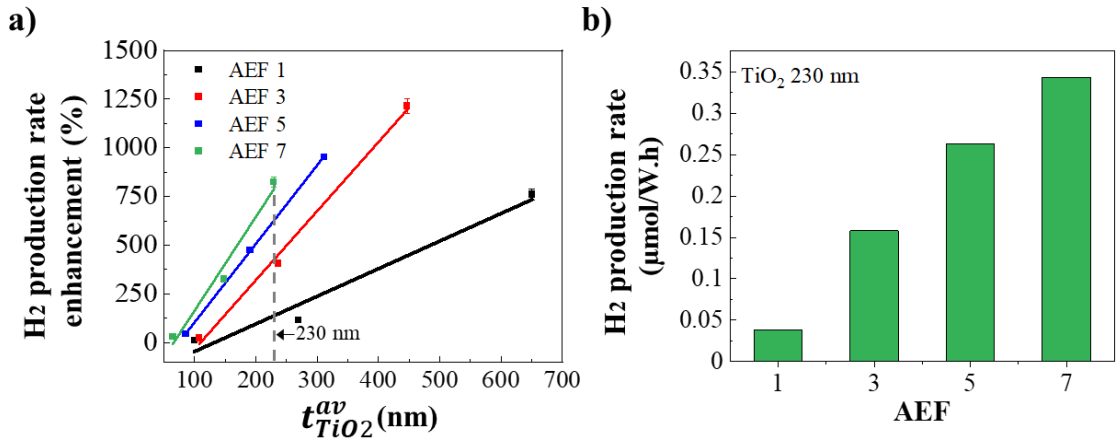

Figure 9. *(a) H_2 production rate enhancement as a function of the TiO_2 average thickness (t_{TiO2}^{av}) for flat and 3D photocatalysts with AEFs of 3, 5 and 7. Values are compared to the H_2 production rate of the reference sample A1-T2. Solid lines are obtained by linear regression.*

(b) Determined impact of AEF on the H_2 production rate for a 3D photocatalyst with a t_{TiO2}^{av} of 230 nm (rate normalized per light flux and surface area).

Figure 9a plots the percentage of the H_2 production rate enhancement compared to planar topology as a function of t_{TiO2}^{av} (*x*-axis) and the AEF (different colored lines). The surface area enlargement clearly boosts the photocatalytic activity, which leads to a remarkable enhancement of the H_2 production rate of 1214% compared to the planar topology. A higher enhancement would be expected for the 3D photocatalysts with an AEF of 5 and 7, since the availability of the sites that conduct the water-splitting reaction is higher. However, it is the photocatalyst with an AEF = 3 that exhibits a higher photocatalytic performance; this behavior can be ascribed to the semiconductor layer uniformity. For samples A5-T3 and A7-T3, the thickness layer variation along the microcavities is high (246-1105 nm and 107-1171 nm) and the enhancement is 956 and 823%, respectively. However, for sample A3-T3, the thickness variation is lower, from 454 to 1174 nm, and the enhancement is notably higher, at 1214%. This remarkable enhancement of a 3D photocatalyst with respect to a planar topology surpassed the expected results, where the efficiency was expected to be directly proportional to the surface area. This establishes that higher efficiencies can be achieved by increasing the AEF when a nearly conformal TiO_2 layer with a minimum thickness of 200 to 300 nm is deposited. Based on the behavior of the AEF on the H_2 production rate, **Figure 9b** shows the predicted H_2 production rate for a conformal TiO_2 layer with a thickness of 230 nm for 3D photocatalysts when varying the AEF: the H_2 production is enhanced by factors of 4, 7 and 9 for AEF values of 3, 5 and 7, respectively, when compared to a photocatalyst with an AEF of 1. This indicates that when microstructures with a higher aspect ratio ≥1.4 and a conformal TiO_2 layer are deposited, H_2 production linearly follows surface augmentation.

To measure the AEF, cyclic voltammetry experiments were carried out on 3D photocatalysts previously sputtered with Au. Thus, conforming electrodes have an entirely

electrochemically-active surface areas; therefore, the 3D microstructures and the surface roughness are inherent to the different TiO_2 thicknesses. The augmentation of the electrochemically active surface areas (AEF_{EAS}) was obtained from the integration of the reduction peak of Au located at 0.85 V vs. Ag/AgCl. Cyclic voltammograms are shown in **Figure S10**. The AEF_{EAS} values for the AEF3 samples with thicknesses of T1, T2 and T3 were 5.78 ± 0.06, 5.54 ± 0.16 and 6.53 ± 0.06, respectively. For the AEF5 samples with thicknesses of T1, T2 and T3, the AEF_{EAS} values were 8.40 ± 0.05, 5.26 ± 0.3 and 7.57 ± 0.04, respectively. For the AEF7 samples with thicknesses of T1, T2 and T3, the AEF_{EAS} values were 8.59 ± 0.18, 9.25 ± 0.03 and 9.59 ± 0.03, respectively. Since a flat photocatalyst with a TiO_2 thickness of 1 µm was used as the reference sample for the AEF_{EAS} calculation, these results not only corroborate that the augmentation of the surface is related to the change in depth of the microcavities but also take into account the roughness and fluctuations associated with the deposited 3D structure of the TiO_2, which therefore creates more electroactive sites where gold oxide is formed and reduced. Note that the thick Au sputtered layer has a roughness that can also contribute to the real surface area augmentation. Therefore, the experimental AEF_{EAS} values are higher than the calculated AEF values from Equation 1, but reflect a good correlation with the theoretical values.

The stability of the photocatalyst is also an important issue in device applications. Therefore, a cyclic H_2 evolution test was carried out for 45 h under light irradiation and under the same conditions as the H_2 production rate tests. The optimal A3-T3 sample was tested for 5 consecutive cycles of 9 h each. The H_2 evolution, shown in **Figure S11,** remained stable, with an average H_2 production of 89.18 µmol W^{-1} by the end of each cycle. Additionally, a small increase was observed after the first cycle, indicating the robustness of the 3D photocatalyst.

A final experiment was carried out to increase the H_2 production rate of the 3D photocatalysts. As previously reported [21], the synthesis of Au NPs on top of the TiO_2 film

allows for light absorption in the visible range (455-475 nm), which has a positive impact on the water-splitting reaction. Au NPs were grown onto the optimal samples A3-T3, A5-T3 and A7-T3. As expected, their H_2 production (**Figure 10a**) increases significantly by factors of 3.3, 3, and 4 for the A3-T3, A5-T3 and A7-T3 samples, respectively, compared to the same samples without Au NPs. Since the improvement is quite similar for the different 3D photocatalysts, it is important to analyze the role of the NPs in relation to the AEF. **Figure 10b-d** shows the images of the microstructures at the top edge of the walls, half-height of the walls and the lower corners of the bottom of the microcavity. The average size of the nanoparticles was 33.6 nm, and the average areal density decreased from 46 to 10 NPs/μm^2 from the top to the bottom of the wall. Furthermore, the NPs located at the half-height, at low height of the walls have an average size of 17 nm, which accounts for a small fraction (< 4%) of the size distribution of the NPs (**Figure S12**). This can be attributed to the diagonal crystallite growth of the walls, where small particles are retained easily during chemical synthesis, compared to horizontal surfaces where any NP size can be easily trapped between the crystallites. Moreover, in **Figure S13,** it can be observed that the NPs are mainly located on the horizontal top surface and on the near vertices with an average areal density of 98 NPs/μm^2, and at the bottom of the microcavities with an average areal density of 31 NPs/μm^2, but not on the walls. This explains why a similar improvement in H_2 production is obtained for all three different microstructures, since the percentage of horizontal surfaces is the same in all the microstructures, with the only changing parameter being the vertical surfaces (walls); therefore, a similar concentration of Au NPs is present in each microstructure.

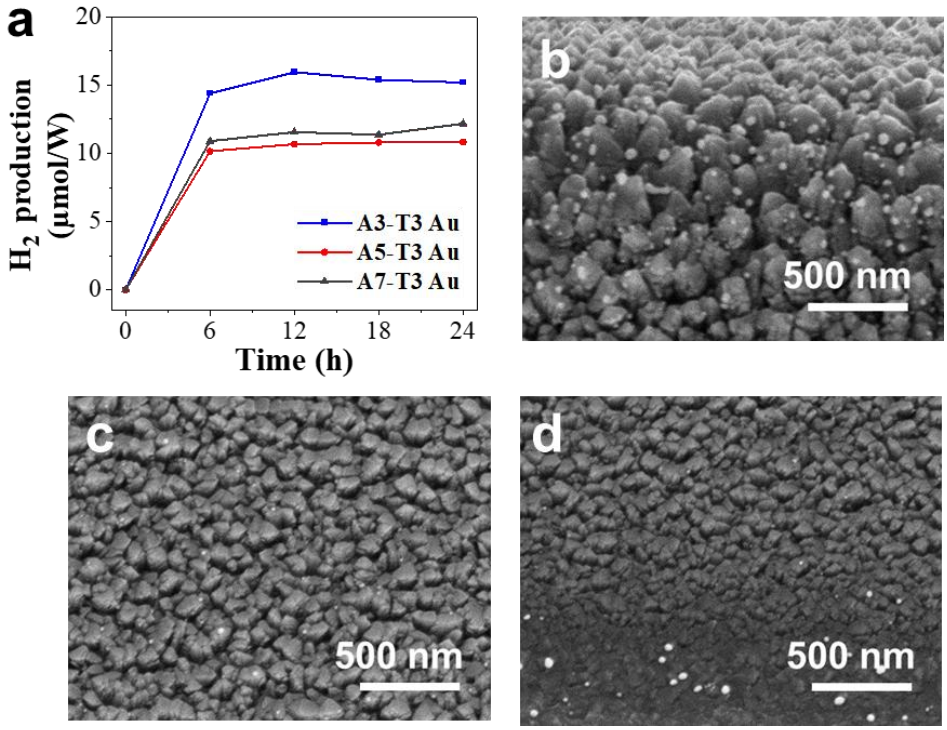

Figure 10. *(a) Hydrogen evolution over 24 h for 3D photocatalyst composed TiO_2 and Au NPs featuring an AEF of 3,5 and AEF 7.SEM images of the top wall (b), wall at the half-height (c), and bottom wall (d) of the 3D photocatalyst TiO_2/Au NPs labeled A3-T3.*

5. Conclusions

The photocatalytic performance for the H_2 production of 3D photocatalysts composed of TiO_2 and TiO_2/Au NPs was reported as a function of semiconductor layer thickness and the aspect ratio relative to specific AEF values. We have demonstrated that, by augmenting the surface area by a factor of 3, H_2 production is enhanced by a factor of 12, due to the increase in active surface area for the water-splitting reaction. Moreover, a supplementary 4-factor H_2 production rate enhancement is achieved by chemical deposition of Au NPs due to the extension of the absorption spectra of the photocatalyst. Furthermore, the results indicate that further developments, such as atomic layer deposition techniques and controlled *in situ* synthesis of metal nanoparticles, can result in major enhancements for higher aspect ratio 3D

photocatalysts. This work provides new insights for the microelectromechanical fabrication of specific areal surface 3D photocatalysts for light-driven H_2 production.

CRediT authorship contribution statement

Maria Isabel Mendoza Diaz: Conceptualization, Methodology, Investigation, Validation, Formal analysis, Writing – original draft, Writing – review & editing, Visualization. **Aurélie Lecestre:** Methodology. **Ludovic Salvagnac:** Methodology. **Botayna Bounor:** Methodology, Formal analysis. **David Pech:** Methodology, Formal analysis. Writing – review & editing. **Mehdi Djafari Rouhani:** Methodology. **Alain Esteve:** Funding acquisition, Formal analysis, Supervision. Writing – review & editing. **Carole Rossi:** Funding acquisition, Formal analysis, Supervision. Writing – review & editing.

Declaration of Competing Interest

The authors declare no competing financial interests.

Acknowledgments

The authors acknowledge the financial support from the European Research Council (H2020 Excellent Science) Researcher Award (Grant No. 832889 – PyroSafe) and from the FEDER/Occitanie Region (Grant H2VERT/HYPHY). This work was also supported by the LAAS-CNRS technology platform, a member of the Renatech network. The authors also thank Dr. Hicham Jabraoui from LAAS, University of Toulouse and Dr. Kui Tan from the Department of Materials Science and Engineering, University of Texas at Dallas, Richardson, TX (USA) for their help in preparing this work: calculation of AEF for the former and performing the XPS analysis for the latter.

Appendix A. Supplementary File

Electronic supplementary information available: details of the fabrication processes and characterization of methods, additional microscopic characterization and photocatalytic and electrochemical experiments, quantum efficiency calculation methods.

References

[1] Barreto, L., Makihira, A., & Riahi, K. (2003). The hydrogen economy in the 21st century: a sustainable development scenario. International Journal of Hydrogen Energy, 28(3), 267-284. https://doi.org/10.1016/S0360-3199(02)00074-5

[2] Crabtree, G. W., Dresselhaus, M. S., & Buchanan, M. V. (2004). The hydrogen economy. Physics today, 57(12), 39-44.

[3] Dotan, H., Landman, A., Sheehan, S. W., Malviya, K. D., Shter, G. E., Grave, D. A., … Grader, G. S. (2019). Decoupled hydrogen and oxygen evolution by a two-step electrochemical–chemical cycle for efficient overall water splitting. Nature Energy, 4(9). https://doi.org/10.1038/s41560-019-0462-7

[4] Fujishima, A., & Honda, K. (1972). Electrochemical photolysis of water at a semiconductor electrode. Nature, 238(5358), 37–38. https://doi.org/10.1038/238037a0

[5] Borgarello, E., Kiwi, J., Pelizzetti, E., Visca, M., & Grätzel, M. (1981). Photochemical cleavage of water by photocatalysis. Nature, 289(5794), 158–160. https://doi.org/10.1038/289158a0

[6] Chen, X., Shen, S., Guo, L., & Mao, S. S. (2010). Semiconductor-based photocatalytic hydrogen generation. Chemical Reviews, 110(11), 6503–6570. https://doi.org/10.1021/cr1001645

[7] Cure, J., Cocq, K., Nicollet, A., Tan, K., Hungria, T., Assie-Souleille, S., … Rossi, C. (2020). A Beehive Inspired Hydrogen Photocatalytic Device Integrating a Carbo-Benzene Triptych Material for Efficient Solar Photo-Reduction of Seawater. Advanced Sustainable Systems, 4(9). https://doi.org/10.1002/adsu.202000121

[8] Iachella, M., Cure, J., Djafari Rouhani, M., Chabal, Y., Rossi, C., & Estève, A. (2018). Water Dissociation and Further Hydroxylation of Perfect and Defective Polar ZnO Model Surfaces. Journal of Physical Chemistry C, 122(38), 21861–21873. https://doi.org/10.1021/acs.jpcc.8b04967

[9] Maeda, K., Teramura, K., Lu, D., Takata, T., Saito, N., Inoue, Y., & Domen, K. (2006). Photocatalyst releasing hydrogen from water. Nature, 440(7082), 295. https://doi.org/10.1038/440295a

[10] Ye, S., Wang, R., Wu, M. Z., & Yuan, Y. P. (2015). A review on g-C 3 N 4 for photocatalytic water splitting and CO 2 reduction. Applied Surface Science, 358, 15–27. https://doi.org/10.1016/j.apsusc.2015.08.173

[11] Ye, S., Wang, R., Wu, M. Z., & Yuan, Y. P. (2015). A review on g-C 3 N 4 for photocatalytic water splitting and CO 2 reduction. Applied Surface Science, 358, 15–27. https://doi.org/10.1016/j.apsusc.2015.08.173

[12] Xu, D., Hai, Y., Zhang, X., Zhang, S., & He, R. (2017). Bi 2 O 3 cocatalyst improving photocatalytic hydrogen evolution performance of TiO 2. Applied Surface Science, 400, 530–536. https://doi.org/10.1016/j.apsusc.2016.12.171

[13] Abdi, F. F., Han, L., Smets, A. H. M., Zeman, M., Dam, B., & Van De Krol, R. (2013). Efficient solar water splitting by enhanced charge separation in a bismuth

vanadate-silicon tandem photoelectrode. Nature Communications, 4. https://doi.org/10.1038/ncomms3195

[14] Fajrina, N., & Tahir, M. (2019). A critical review in strategies to improve photocatalytic water splitting towards hydrogen production. International Journal of Hydrogen Energy, 44(2), 540–577. https://doi.org/10.1016/j.ijhydene.2018.10.200

[15] Goto, Y., Hisatomi, T., Wang, Q., Higashi, T., Ishikiriyama, K., Maeda, T., … Domen, K. (2018). A Particulate Photocatalyst Water-Splitting Panel for Large-Scale Solar Hydrogen Generation. Joule, 2(3), 509–520. https://doi.org/10.1016/j.joule.2017.12.009

[16] Cure, J., Cocq, K., Mlayah, A., Hungria, T., Alphonse, P., Chabal, Y. J., … Rossi, C. (2019). A triptych photocatalyst based on the Co-Integration of Ag nanoparticles and carbo-benzene dye into a TiO2 thin film. International Journal of Hydrogen Energy, 44(48), 26347–26360. https://doi.org/10.1016/j.ijhydene.2019.08.126

[17] Veziroglu, S., Ullrich, M., Hussain, M., Drewes, J., Shondo, J., Strunskus, T., … Aktas, O. C. (2020). Plasmonic and non-plasmonic contributions on photocatalytic activity of Au-TiO2 thin film under mixed UV–visible light. Surface and Coatings Technology, 125613. https://doi.org/10.1016/j.surfcoat.2020.125613

[18] Eustache, E., Tilmant, P., Morgenroth, L., Roussel, P., Patriarche, G., Troadec, D., … Lethien, C. (2014). Silicon-microtube scaffold decorated with anatase TiO2 as a negative electrode for a 3D litium-ion microbattery. Advanced Energy Materials, 4(8), 1–11. https://doi.org/10.1002/aenm.201301612

[19] Wang, J., Shao, H., Ren, S., Hu, A., & Li, M. (2021). Fabrication of porous Ni-Co catalytic electrode with high performance in hydrogen evolution reaction. Applied Surface Science, 539. https://doi.org/10.1016/j.apsusc.2020.148045

[20] Störmer, M., Blawert, C., Hagen, H., Heitmann, V., & Dietzel, W. (2007). Structure and corrosion of magnetron sputtered pure Mg films on silicon substrates. Plasma Processes and Polymers, 4(S1), S557-S561. https://doi.org/10.1002/ppap.200731405

[21] Mendoza-Diaz, M. I., Cure, J., Rouhani, M. D., Tan, K., Patnaik, S. G., Pech, D., … Estève, A. (2020). On the UV-Visible Light Synergetic Mechanisms in Au/TiO2Hybrid Model Nanostructures Achieving Photoreduction of Water. Journal of Physical Chemistry C, 124(46), 25421–25430. https://doi.org/10.1021/acs.jpcc.0c08381

[22] Jansen, H., De Boer, M., Legtenberg, R., & Elwenspoek, M. (1995). The black silicon method: A universal method for determining the parameter setting of a fluorine-based reactive ion etcher in deep silicon trench etching with profile control. Journal of Micromechanics and Microengineering, 5(2), 115–120. https://doi.org/10.1088/0960-1317/5/2/015

[23] Silva Junior, E., La Porta, F. A., Liu, M. S., Andrés, J., Varela, J. A., & Longo, E. (2015). A relationship between structural and electronic order-disorder effects and optical properties in crystalline TiO2 nanomaterials. Dalton Transactions, 44(7), 3159–3175. https://doi.org/10.1039/c4dt03254c

[24] Cottre, T., Fingerle, M., Kranz, M., Mayer, T., Kaiser, B., & Jaegermann, W. (2021). Interaction of Water with Atomic Layer Deposited Titanium Dioxide on p- Si Photocathode: Modeling of Photoelectrochemical Interfaces in Ultrahigh Vacuum with Cryo- Photoelectron Spectroscopy. *Advanced Materials Interfaces*, *8*(11), 2002257. https://doi.org/10.1002/admi.202002257

[25] Trasatti, S., & Petrii, O. A. (1991). International Union of Pure and Applied Chemistry Physical Chemistry Division Commission on Electrochemistry: Real Surface Area Measurements in Electrochemistry. Pure and Applied Chemistry, 63(5), 711–734. https://doi.org/10.1351/pac199163050711

[26] Lukaszewski, M., Soszko, M., & Czerwiński, A. (2016). Electrochemical methods of real surface area determination of noble metal electrodes - an overview. International Journal of Electrochemical Science, Vol. 11, pp. 4442–4469. https://doi.org/10.20964/2016.06.71